MDPI

Article

Plasmon-Enhanced CO$_2$ Reduction to Liquid Fuel via Modified UiO-66 Photocatalysts

Alaa Elsafi [1,2,†], Zeineb Theihmed [1,†], Amna Al-Yafei [3], Alaa Alkhateeb [1], Ahmed Abotaleb [1], Muhammad Anwar [1], Kamal Mroue [4], Brahim Aissa [1,*] and Alessandro Sinopoli [1,*]

[1] Qatar Environment and Energy Research Institute (QEERI), Hamad Bin Khalifa University (HBKU), Doha P.O. Box 34110, Qatar; aa1702336@student.qu.edu.qa (A.E.); zthiehmed@hbku.edu.qa (Z.T.); aalkhateeb@hbku.edu.qa (A.A.); muanwar@hbku.edu.qa (M.A.)

[2] Materials Science and Technology Graduate Program, Department of Physics and Materials Science, Qatar University, Doha P.O. Box 2713, Qatar

[3] Department of Chemistry and Earth Sciences, College of Arts and Sciences, Qatar University, Doha P.O. Box 2713, Qatar; aa2003453@student.qu.edu.qa

[4] HBKU Core Laboratories, Hamad Bin Khalifa University (HBKU), Doha P.O. Box 34110, Qatar; kmroue@hbku.edu.qa

[*] Correspondence: baissa@hbku.edu.qa (B.A.); alessandro.sinopoli@unime.it (A.S.)

[†] These authors contributed equally to this work.

Abstract: Metal–organic frameworks (MOFs) have emerged as versatile materials with remarkably high surface areas and tunable properties, attracting significant attention for various applications. In this work, the modification of a UiO-66 MOF with metal nanoparticles (NPs) is investigated for the purpose of enhancing its photocatalytic activity for CO$_2$ reduction to liquid fuels. Several NPs (Au, Cu, Ag, Pd, Pt, and Ni) were loaded into the UiO-66 framework and employed as photocatalysts. The synergistic effects of plasmonic resonance and MOF characteristics were investigated to improve photocatalytic performance. The synthesized materials were characterized by X-ray powder diffraction (XRD), scanning electron microscopy (SEM), transmission electron microscopy (TEM), and X-ray photoelectron spectroscopy (XPS), confirming the successful integration of metal NPs onto the UiO-66 framework. Morphological analysis revealed distinct distributions and sizes of NPs on the UiO-66 surface for different metals. Photocatalytic CO$_2$ reduction experiments demonstrated enhanced activity of plasmonic MOFs, yielding methanol and ethanol. The findings revealed by this study provide valuable insights into tailoring MOFs for improved photocatalytic applications through the incorporation of plasmonic metal nanoparticles.

Keywords: metal–organic frameworks; photoconversion; methanol; plasmonic nanoparticles

1. Introduction

Metal–organic frameworks (MOFs) can be described as crystalline networks of organic building units, which are ligands, linked through strong coordination bonds with inorganic metal ions or clusters [1]. This coordination results in a high-surface-area porous structure with tunable chemical and physical properties [2–4]. MOFs represent a fascinating and rapidly evolving class of porous materials that have garnered significant attention from the scientific community in recent years. The unique combination of organic and inorganic components allows for precise control over their structural and chemical properties. MOFs are characterized by their extremely high surface areas, tunable porosity, and a wide range of potential applications, making them a subject of extensive research and innovation [5–8].

The synthesis of MOFs is versatile, with an ever-expanding library of both metal ions and organic ligands, enabling the design of MOFs with tailored properties for specific applications. This flexibility has led to a broad array of MOFs, each with distinct properties, such as varying pore sizes, shapes, and chemical functionalities. As a result, MOFs have found applications in fields as diverse as gas storage and separation, catalysis, drug delivery, sensing, and environmental remediation, to name just a few [9,10]. One of the remarkable characteristics of MOFs is that they allow for loading guest materials to achieve novel properties in several applications, such as photocatalysis and sensors.

When compared to traditional photocatalysts, such as TiO_2 or $g-C_3N_4$, MOFs stand out as highly versatile materials. Indeed, unlike conventional photocatalysts, MOFs are characterized by an exceptionally high surface area and porosity, providing abundant active sites that enhance the adsorption and diffusion of reactants [11,12]. Their modular nature allows for the precise tuning of chemical and structural properties, enabling control over critical factors such as band gaps, light absorption, and catalytic activity. MOFs can be engineered to effectively harness visible light while mitigating charge recombination, addressing two major limitations of traditional materials [10,11,13]. Moreover, their ability to incorporate functional components, such as metal nanoparticles or quantum dots, creates synergistic effects that improve charge separation and light utilization. Advances in MOF design have also enhanced their thermal, chemical, and photostability, ensuring they maintain efficiency over prolonged usage.

While pristine MOFs face challenges such as limited light absorption and carrier recombination [14,15], these shortcomings can be overcome by integrating guest materials into their matrices, unlocking promising photoactivity and expanding their application potential. Among the different guest materials, inorganic metal nanoparticles attract particular attention, mainly due to their unique properties on the nanoscale. Noble metal nanoparticles that can interact with the visible and infrared regions of light are called plasmonic nanoparticles [16–18]. Due to their nanoscale dimensions, the collective conduction electronic oscillation of the metal is confined to the nanoparticle surface, resulting in localized surface plasmon resonance (LSPR). As a result of this phenomenon, metal nanoparticles acquire two main unique optical properties, namely strong light absorption and an intense electromagnetic field [19]. Given the outstanding properties of plasmonic metal NPs and MOFs on their own, it has been proposed that plasmonic MOFs can offer a promising platform for enhanced photocatalytic activity [20]. Among the different MOF families, UiO-66 has been employed as a host to confine and provide stability to metal nanoparticles for improved photocatalytic activity. Zhao et al. reported enhanced photocatalytic activity of producing NH_3 from N_2 reduction using a Au@UiO-66 photocatalyst [21]. In addition, plasmonic NPs and MOFs can also be simultaneously incorporated with molecular photocatalysts to boost their intrinsic photocatalytic activity in a two-pronged approach.

Among the different applications of MOFs in photocatalysis, CO_2 photoreduction represents a transformative process that addresses climate and energy challenges by converting carbon dioxide, a major greenhouse gas, into valuable fuels like methanol and ethanol using sunlight [22–25]. It mitigates climate change by reducing atmospheric CO_2 levels, supports renewable energy production by utilizing abundant solar energy, and promotes a circular carbon economy through resource recovery and sustainable fuel generation. The process drives innovation in materials science, offers economic potential, and aligns with global decarbonization goals, providing a localized renewable energy source. By integrating environmental, economic, and technological benefits, CO_2 photoreduction plays a pivotal role in creating a sustainable and low-carbon future [22].

MOFs are considered desirable photocatalysts for CO_2 conversion due to their superior CO_2 capture capacity, unique reticular structures, and photoelectronic properties [12,26–28].

Recent progress in MOF-based photocatalysts for CO_2 reduction has focused on homometallic and heterometallic MOFs [29,30]. For instance, a CO_2-to-CO conversion photocatalyst $ReI(CO)_3(BPYDC)Cl$ can be covalently attached to a zirconium MOF and further coated onto plasmonic Ag nanocubes ($Ag \subset Re3$–MOF) to exhibit enhanced CO_2 conversion [31]. Thus, coupling with Ag nanocubes allows the photoactive Re centers to be spatially localized close to the intense electric field generated by the plasmonic nanoparticles, which can be absorbed by ReTCs to enhance photocatalytic activities. As a result, the $Ag \subset Re3$–MOF exhibits a 7-fold enhancement in photocatalytic activity than the Re3–MOF control. Another study reported by Robatjazi et al. focused on the synthesis of an MIL-53 MOF doped with Al NP, revealing that the MOF coating boosted the photocatalytic activity of Al NPs towards the reduction of CO_2 by reverse water–gas shift reactions [32].

Among the plethora of MOF structures, UiO-66 is a good support for photocatalytic CO_2 conversion due to its exceptional properties such as high surface area and tunable porosity, which facilitate the adsorption and activation of CO_2 molecules [33,34]. The framework's zirconium-based nodes offer strong Lewis acidic sites that enhance CO_2 binding and activation, which is crucial for initiating reduction reactions [12]. Moreover, the structural stability of UiO-66 under light irradiation and in aqueous environments ensures its durability during photocatalytic processes. The modular nature of UiO-66 allows for functionalization with light-absorbing components, further improving its efficiency in photocatalysis. These characteristics make UiO-66 and its derivates an ideal platform for supporting active species like metal NPs in CO_2 photoreduction. Moreover, Wang et al. developed a photoinduction method to synthesize Cu single atoms on a $UiO-66-NH_2$ support to enhance the photoreduction of CO_2 to liquid fuels. The evolution rates for the solar-driven CO_2 conversion under $Cu\ SAs/UiO-66-NH_2$ to methanol and ethanol were recorded as 5.33 and 4.22 $\mu mol\,h^{-1}\,g^{-1}$, respectively, which are higher than those of pristine $UiO-66-NH_2$ and Cu nanoparticles/$UiO-66-NH_2$ [35]. Liquid fuels are used in various energy applications, contributing to the efficiency of energy systems and sustainability. CO_2 photoconversion into liquid fuels such as methanol is considered as a promising energy storage method due to the high energy density and versatility of liquid fuels [36].

In this work, a UiO-66 MOF was selected as a host for loading different metal nanoparticles to study and compare the effects of plasmon resonance on photocatalytic activity. Au, Cu, Ag, Pd, Pt, and Ni nanoparticles were loaded into the UiO-66 framework and used as photocatalysts for the conversion of CO_2 to liquid fuels. This study aims to advance the understanding of plasmonic MOFs, defined as plasmonic metal nanoparticles (NPs) embedded within a metal–organic framework (MOF) matrix [37] and their potential in sustainable energy applications by offering a comparative analysis of various metal nanoparticles integrated with UiO-66 for enhanced photocatalytic performance. By systematically investigating these combinations, the research seeks to identify the most effective strategies for optimizing MOF-based photocatalysts for CO_2 conversion, contributing to the broader goal of developing efficient and sustainable methods for energy storage and utilization.

2. Results and Discussion

The metal NP@UiO-66 catalysts were successfully synthesized by loading different metal nanoparticles via the chemical reduction approach. To explore the crystallinity of the modified UiO-66, powder XRD analysis was carried out for UiO-66 samples loaded with six different metals, namely gold, copper, silver, palladium, platinum, and nickel. The powder XRD analysis in Figure 1 reveals that after doping with the metal NPs, the XRD patterns of all the samples retain the pattern of pristine UiO-66. The common main peak at around $2\theta = 7.37°$ may indicate that the loading has virtually no effect on the crystalline structure of the UiO-66. Moreover, the absence of metallic peaks is attributed to the low

metal loading and might indicate a high dispersion of the NP species. For instance, no additional XRD peaks have been reported for Cu@UiO-66-NH$_2$, with a metal loading <1%.
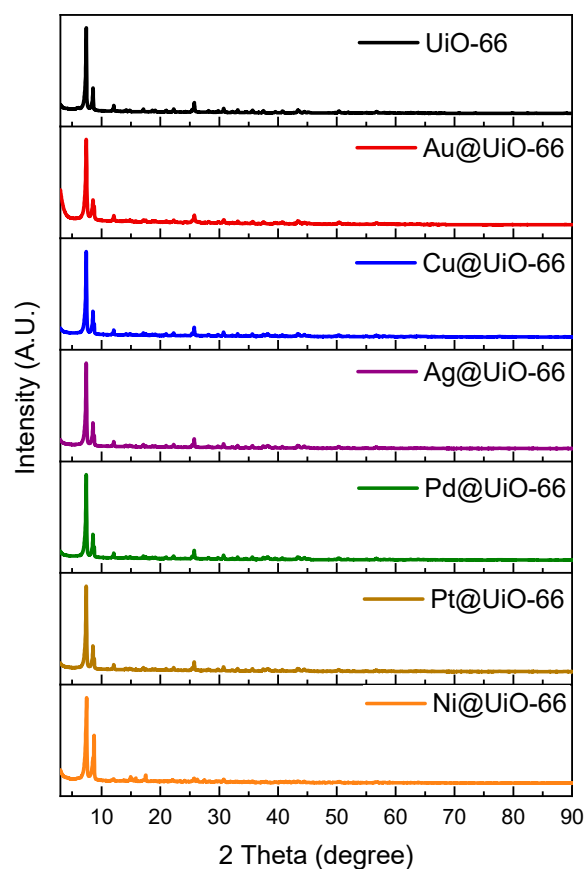

Figure 1. XRD patterns of the pristine and metal-doped UiO-66.

TEM and SEM analyses were performed to study the morphology and composition of the modified UiO-66. Figure 2 shows the typical TEM images along with the associated EDS mapping for each metal sample. In general, the elemental mapping clearly reveals the successful integration of all targeted metal nanoparticles into the UiO-66, indicating successful reduction reactions. However, the size and distribution of the metal nanoparticles are quite different. It can be observed that for Au, Cu, Pd, and Pt, the metal nanoparticles are evenly distributed over the MOF particle surfaces, with relatively similar particle sizes. However, for Ni, the nanoparticles are less evenly distributed, concentrated on some MOF particles and absent from others. In the case of silver, the nanoparticles tend to agglomerate and form larger chunks. The inclusion of Ag within the UiO-66 scaffold has been discussed by Wang et al., showing that the aggregation of Ag clusters are more prone to aggregation due to weaker interactions with the UiO-66 framework, limiting their catalytic performance [38].

The morphological characteristics and the percentage of loading of the different metal NPs on UiO-66 were examined by SEM and are shown in Figure S1. In general, the MOF maintains the same spherical particle morphology as the original UiO-66 in all samples. The SEM and EDS analyses verified the loading of the different metals (as shown in Figure S2), where Pt exhibits the largest loading with 1.17 wt. % and Pd the lowest one with 0.42 wt. %. In addition, Au, Cu, Ag, and Ni have a loading of 0.74 wt. %, 1.07 wt. %, 0.81 wt. %, and 0.55 wt. %, respectively.

XPS measurements of the samples were carried out to investigate the metal states in the UiO-66 support. Figure 3a shows the high-resolution XPS spectrum of Au@UiO-66,

which displays the Au 4f doublet at 83.9 eV for Au $4f_{7/2}$ and at 88.5 eV for Au $4f_{5/2}$. This indicates the presence of mainly Au metallic species. Similar results were observed for Pt, where the high-resolution Pt 4f XPS spectrum shown in Figure 3f is convoluted into two pairs of peaks. The spin–orbit separation of the Pt $4f_{7/2}$ and Pt $4f_{5/2}$, which correspond to Pt, appeared at 71.0 eV and 75.1 eV and are characteristic of Pt^0. However, Cu, Pd, and Ni samples reveal the presence of mainly metal (II) species, indicating the oxidation of the samples, as shown in Figure 3b, Figure 3e, and Figure 3d, respectively. For the Ag@UiO-66 samples, peaks with binding energies at 369 eV and 375 eV correspond to Ag^0, as shown in Figure 3c. However, the spectrum also shows distinguished peaks at 368.6 eV and 374.4 eV, which are assigned to Ag oxide, revealing the partial oxidation of the sample. For all samples, Zr, C, and O elements were detected, which demonstrates the successful preparation of metal NP@UiO-66.
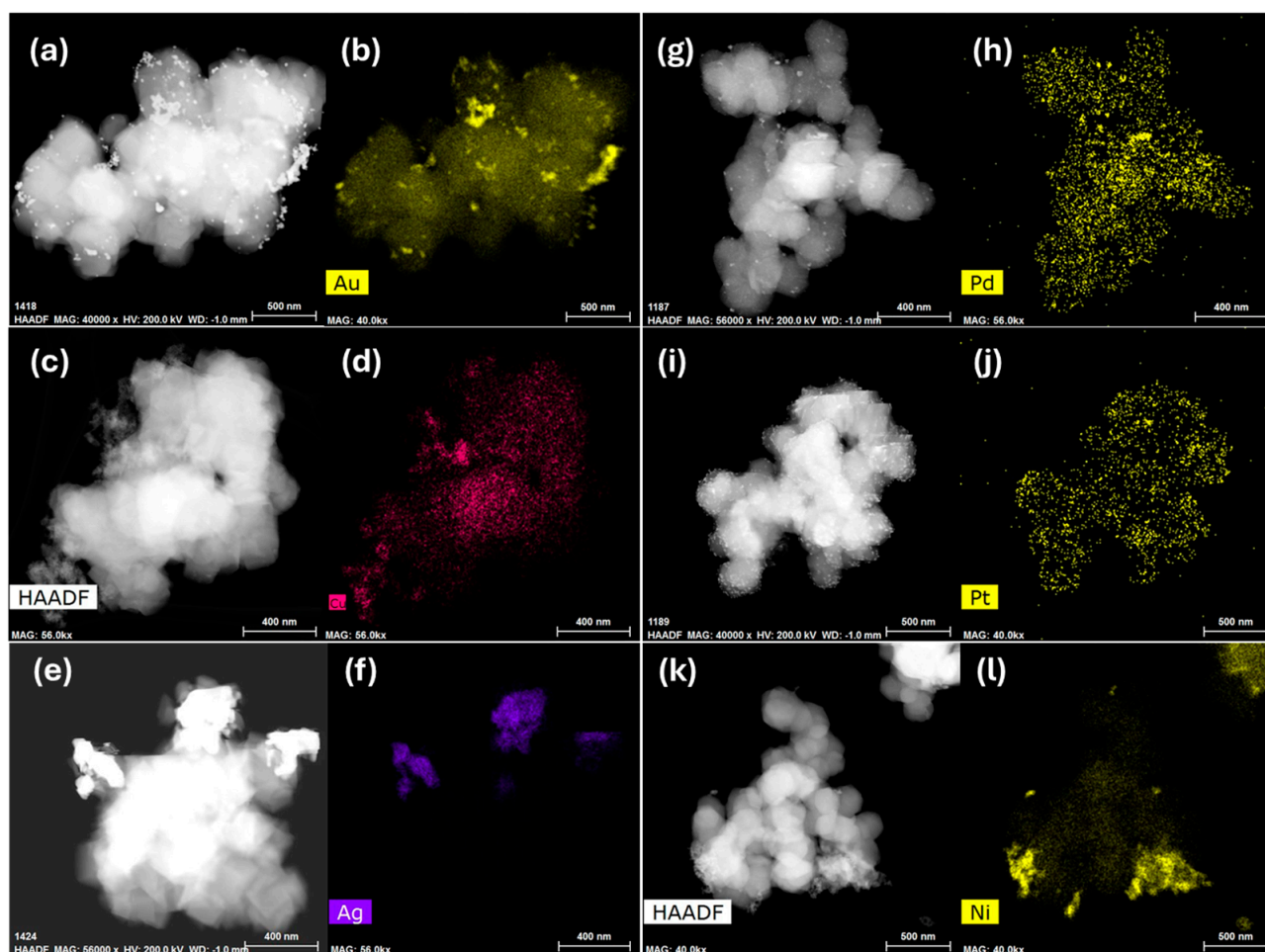
Figure 2. TEM images and EDS mapping of (**a**) and (**b**) Au@UiO-66; (**c**) and (**d**) Cu@UiO-66; (**e**) and (**f**) Ag@UiO-66; (**g**) and (**h**) Pd@UiO-66; (**i**) and (**j**) Pt@UiO-66; (**k**) and (**l**) Ni@UiO-66, respectively.

Pore size distribution, as well as N_2 adsorption–desorption isotherms of pristine and modified UiO-66 samples, examined at 77 K, are displayed in Figure 4, and the corresponding values are listed in Table 1, from which S_{BET} and the pore diameter of the investigated samples were determined. All synthesized samples displayed type I isotherms based on the IUPAC classification, which revealed their microporous nature.
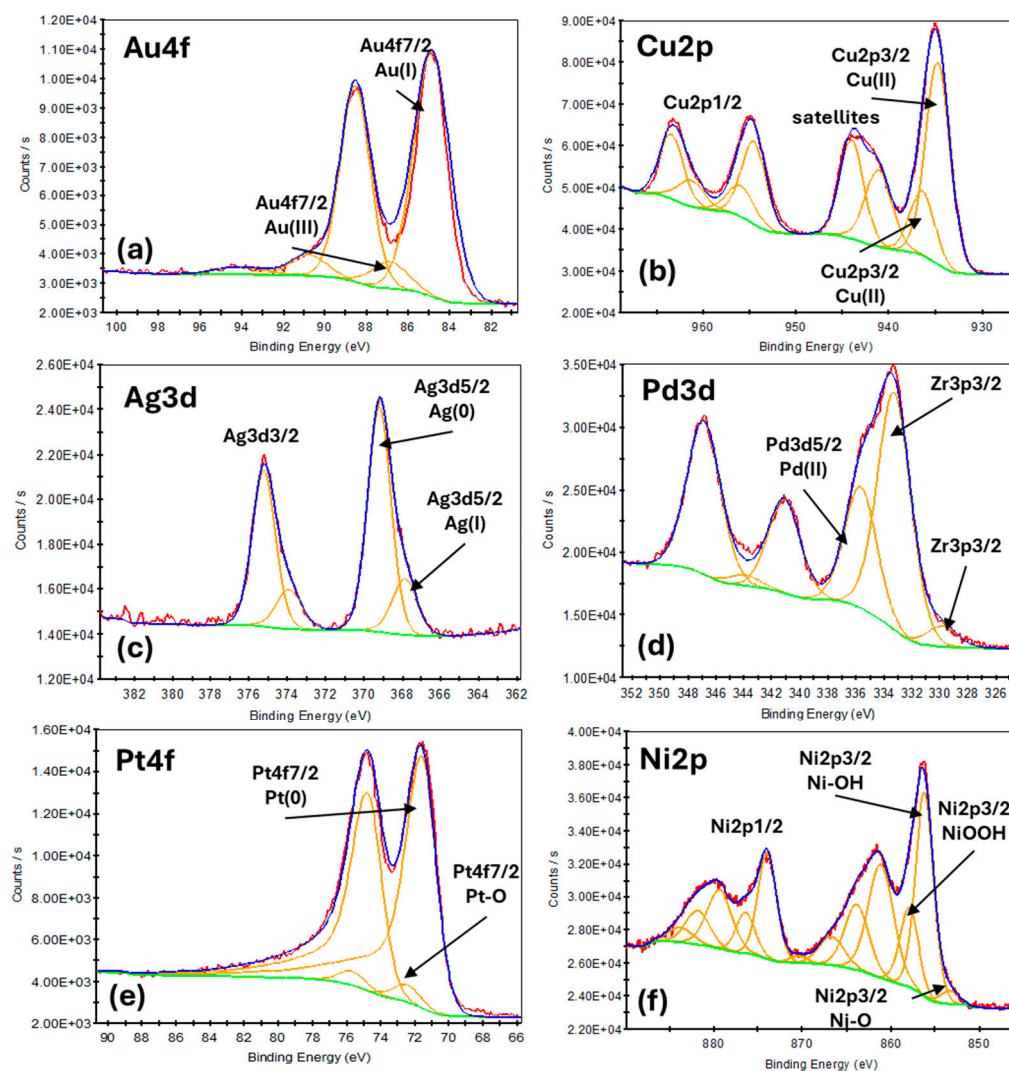
Figure 3. High-resolution XPS spectra for (**a**) Au@UiO-66, (**b**) Cu@UiO-66, (**c**) Ag@UiO-66, (**d**) Ni@UiO-66, (**e**) Pd@UiO-66, and (**f**) Pt@UiO-66.
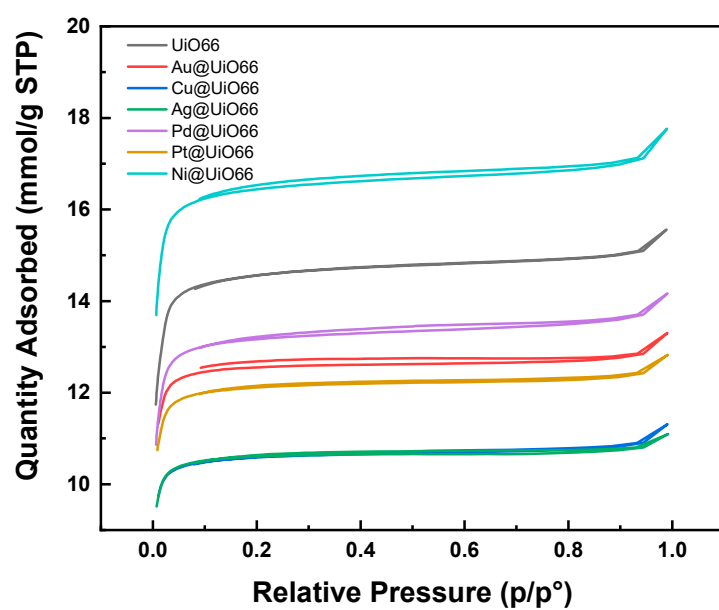
Figure 4. N_2 adsorption–desorption isotherms of the metal-doped UiO-66.

Table 1. BET measurements of pristine and modified UiO-66 samples.

Sample	BET Surface Area, S_{BET} [m^2/g]	Langmuir Surface Area [m^2/g]	Micropore Area, [m^2/g]	Total Pore Volume, V_t [cm^3/g]	Average Pore Size [nm]
UiO-66	1355	1436	1268	0.4946	3.55
Au@UiO-66	1172	1234	1130	0.4349	3.76
Cu@UiO-66	985	1041	944	0.3619	4.03
Ag@UiO-66	991	1041	954	0.3626	3.21
Pd@UiO-66	1231	1297	1163	0.4499	3.38
Pt@UiO-66	1130	1192	1080	0.4150	3.51
Ni@UiO-66	1532	1618	1444	0.563	3.46

Figure 5 summarizes the average pore size and S_{BET} values of pristine and modified UiO-66 samples. Ni@UiO-66 has the largest surface area of 1532 m^2/g, which could represent a preferential factor for CO$_2$ adsorption, followed by pristine UiO-66, Pd@UiO-66, Au@UiO-66, Pt@UiO-66, then Ag@UiO-66. Contrarily, Cu@UiO-66 exhibited the smallest surface area (985 m^2/g), which may decrease its activity towards CO$_2$ reduction.
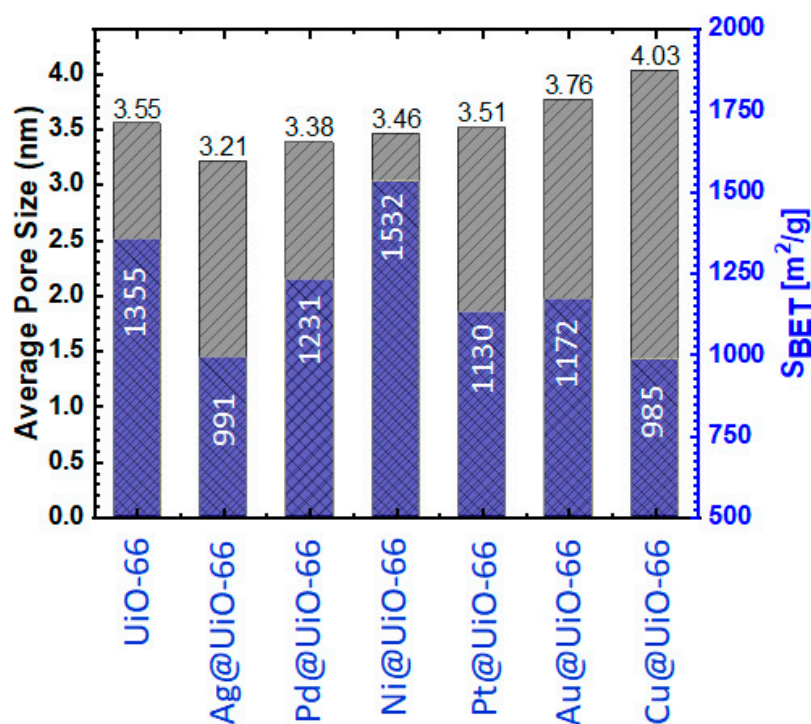
Figure 5. Histogram summarizing the average pore size and S_{BET} values of pristine and modified UiO-66 samples.

It is well known that the surface area of MOFs can be significantly influenced by the size distribution of incorporated metal NPs. Smaller NPs typically exhibit a higher surface area-to-volume ratio, which may enhance the effective surface area of the MOF when well dispersed. Conversely, larger or agglomerated NPs can obstruct the MOF's pores, thereby reducing its accessible surface area. Additionally, the interaction between the metal NPs and the MOF may lead to synergistic effects that alter surface properties, impacting overall performance. The size and distribution of the NPs also play a key role in maintaining the structural integrity of the MOF; excessive distortion or collapse can adversely affect its surface area. Furthermore, the presence of metal NPs can modify the functional groups

on the MOF's surface, influencing its adsorption characteristics and the availability of active sites for reactions. Ongoing work aims to comprehensively understand how the size distribution of our NPs is essential for optimizing the surface area and performance of MOFs in this specific application.

The CO_2 adsorption capacity of the MOFs decorated with metal NPs was measured using an ASAP 2420 instrument from Micromeritics at 21 °C. Prior to measurements, samples were dried at 90 °C for 30 min, followed by degassing at 150 °C for 4 h under vacuum to eliminate CO_2, water, and any other impurities. Subsequently, CO_2 (purity 99.999%) was purged until reaching equilibrium at a constant temperature of 21 °C. Figure 6 illustrates the CO_2 adsorption isotherms for UiO-66, Au@UiO-66, Cu@UiO-66, Ag@UiO-66, Pd@UiO-66, Pt@UiO-66, and Ni@UiO-66 at room temperature. The physical adsorption of CO_2 was examined up to 1.0 partial pressure, with intervals of over 70 points, to capture CO_2 uptake at low pressures. Interestingly, all MOFs exhibit a similar trend, with Ni@UiO-66 demonstrating the highest CO_2 capacity at 2.27 mmol/g, attributed to its relatively larger surface area and its total pore volume. Following Ni@UiO-66, Pd@UiO-66 exhibits a capacity of 1.66 mmol/g, followed by Cu@UiO-66 (1.55 mmol/g), UiO-66 (1.43 mmol/g), Au@UiO-66 (1.42 mmol/g), Pt@UiO-66 (1.38 mmol/g), and Ag@UiO-66 (1.30 mmol/g). The enhanced uptake observed for Ni@UiO-66 is ascribed to its nickel content and its affinity for CO_2 absorption at room temperature, along with its microporous characteristics facilitating better mass transfer rates. Interestingly, a computational study reported by Wang et al. indicates that metals like Ni, Cu, and Pd, facilitate notable charge transfer to the MOF, creating electron-deficient sites that can act as Lewis acids [38]. This charge redistribution is crucial for CO_2 adsorption and activation, which is corroborated by the enhanced CO_2 capture in Ni-, Pd-, and Cu-modified UiO-66 structures in Figure 6. Ni@UiO-66, in particular, exhibited the highest CO_2 adsorption capacity, attributed to its high surface area and electron-donating properties, which aligns with the DFT analysis by Wang, suggesting Ni's substantial charge transfer and stability in catalytic applications. Furthermore, as observed for the BET trend, the CO_2 adsorption profiles come from a combination of morphological and physical factors, such as porosity, affinity between metal and gas, metal dispersion, and particle size.
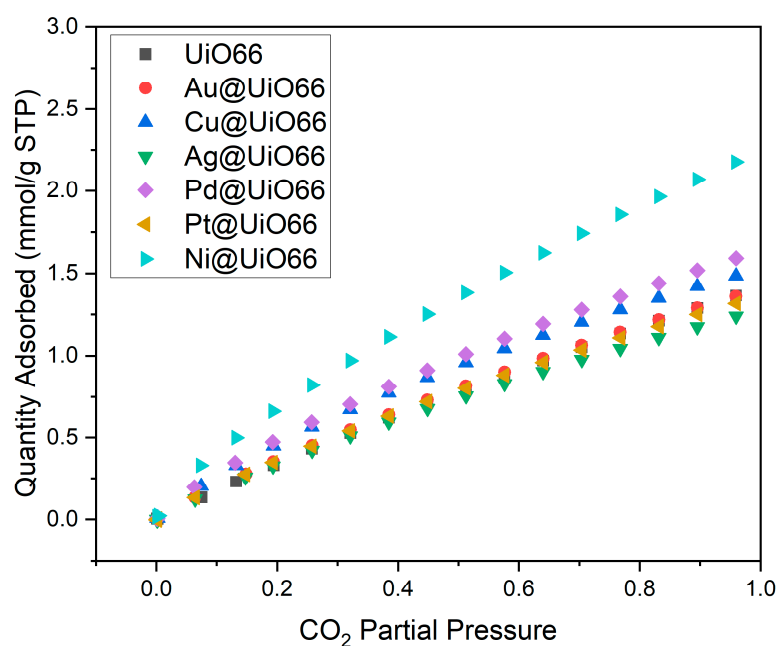

Figure 6. CO_2 adsorption isotherms of investigated samples at 21 °C.

The optical properties of the NP-MOF samples were studied by the DRS–UV–visible technique. Figure 7 depicts the absorbance spectra, whereas the estimation of the bandgap values by the Tauc plot method is depicted in Figure S3. As previously reported in the literature, UiO-66 showed weak absorption in the visible range [39]. The spectrum for Au@UiO-66 (black line) shows significant absorbance in the visible range, with a broad peak around 530 nm. This broad absorption is indicative of the localized surface plasmon resonance (LSPR) of gold nanoparticles, which enhances light absorption and facilitates efficient charge separation and transfer processes. Cu@UiO-66 (red line) also exhibits extended absorption into the visible region, with a notable peak around 600 nm and a tail up to 800 nm. Copper nanoparticles have a distinct plasmonic resonance, although less pronounced than gold, contributing to improved photocatalytic performance through enhanced light absorption. The spectrum for Ag@UiO-66 (blue line) does not display the typical peak around 400 nm characteristic of silver nanoparticle plasmonic resonance; this could be attributed to the large silver particles decorating the MOF structure and their partial oxidation, as observed in the XPS spectra. Pd@UiO-66 (magenta line) and Pt@UiO-66 (green line) both show a slightly extended absorption into the visible range compared to pristine UiO-66, but with no distinct plasmonic peak. In general, palladium and platinum do not exhibit strong plasmonic resonance like Au, Cu, or Ag, which might explain their moderate enhancement in photocatalytic activity. Indeed, their catalytic properties are more related to their chemical activity rather than plasmonic effects. Ni@UiO-66 (orange line) shows some absorption in the visible range but without a pronounced peak, indicating minimal plasmonic resonance effects. Nickel's contribution to photocatalysis is likely through other mechanisms such as enhanced charge separation. Among the metal-decorated catalysts, Au@UiO-66 and Cu@UiO-66 show the most pronounced plasmonic resonance, leading to enhanced light absorption in the visible range. These enhanced optical properties can certainly, but not solely, lead to effective charge separation and extended electron lifetimes, enhancing the catalytic reduction of CO_2 into methanol and ethanol, as observed in the performance data. Understanding these absorption characteristics is crucial in designing and optimizing MOF-based catalysts for efficient solar-driven chemical transformations.
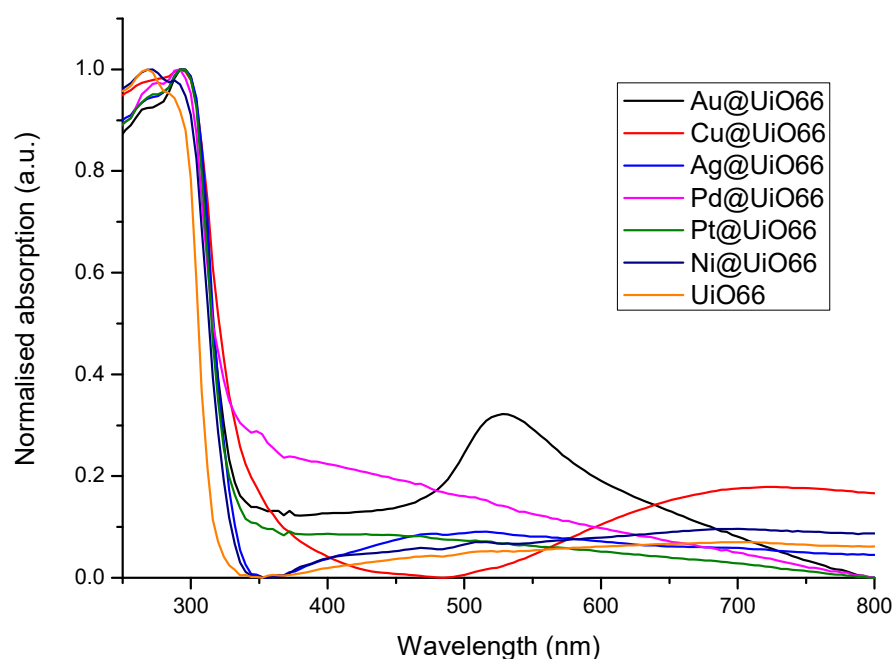

Figure 7. Diffuse reflectance spectra of investigated MOFs.

Photocatalytic Performance

To assess the photocatalytic activities of the as-synthesized samples, we performed the photocatalytic reduction of CO_2 in an aqueous system under visible light irradiation. Table 2 presents the photocatalytic yields for the different MOF catalysts decorated with metallic particles, measured in micromoles per gram per hour (μmol$\cdot$g$^{-1}\cdot$h^{-1}) for methanol and ethanol production. The data highlight the distinct efficiency and selectivity of these catalysts in the photoconversion of CO_2 to valuable liquid fuels. Pure UiO-66 serves as the baseline, showing no methanol yield and a moderate ethanol yield of 6.32 μmol g$_{cat}^{-1}$ h^{-1}. The addition of gold (Au@UiO-66) significantly enhances the methanol yield to 656.54 μmol g$_{cat}^{-1}$ h^{-1} and slightly increases the ethanol yield to 11.01 μmol g$_{cat}^{-1}$ h^{-1}. This dramatic increase in the methanol yield can be attributed to the enhanced light absorption and efficient charge separation facilitated by the gold nanoparticles, promoting the reduction of CO_2 to methanol and ethanol. Copper-decorated UiO-66 (Cu@UiO-66) exhibits a methanol yield of 50.61 μmol g$_{cat}^{-1}$ h^{-1} and the highest ethanol yield among the catalysts at 12.45 μmol g$_{cat}^{-1}$ h^{-1}. Copper's ability to adsorb CO_2 and facilitate the formation of key intermediates like COOH* and CHO* is crucial in this process. Theoretical calculations suggested that the introduction of copper atoms in UiO-66 enhances the conversion of CO_2 to these intermediates, thus boosting the selectivity towards methanol and ethanol [35]. Silver (Ag@UiO-66) shows a moderate methanol yield of 20.26 μmol g$_{cat}^{-1}$ h^{-1} but no ethanol production. The lack of ethanol formation might be due to the silver's catalytic properties, which favor methanol production over ethanol. Palladium (Pd@UiO-66) does not produce methanol but has an ethanol yield of 5.26 μmol g$_{cat}^{-1}$ h^{-1}, indicating its selectivity towards ethanol production, possibly due to its electronic structure and interaction with CO_2 reduction intermediates. Platinum (Pt@UiO-66) exhibits very low yields for both methanol (1.10 μmol g$_{cat}^{-1}$ h^{-1}) and ethanol (0.10 μmol g$_{cat}^{-1}$ h^{-1}), suggesting that while platinum can facilitate some CO_2 reduction, its efficiency is significantly lower compared to other metals. Nickel-decorated UiO-66 (Ni@UiO-66) shows a moderate methanol yield of 43.48 μmol g$_{cat}^{-1}$ h^{-1} but no ethanol yield, indicating a preferential pathway towards methanol production.

Table 2. Photocatalytic yields of methanol and ethanol for the studied catalysts, measured by GC analysis.

| Catalyst	Methanol Yield (μmol g$_{cat}^{-1}$ h^{-1})	Ethanol Yield (μmol g$_{cat}^{-1}$ h^{-1})
UiO-66	0	6.32
Au@UiO-66	656.54	11.01
Cu@UiO-66	50.61	12.45
Ag@UiO-66	20.26	0
Pd@UiO-66	0	5.26
Pt@UiO-66	1.09	0.09
Ni@UiO-66	43.48	0

Overall, the catalytic performance of these MOF-based catalysts varies significantly with the nature of metallic particle used. Gold-decorated UiO-66 stands out for its exceptional methanol yield, while copper-decorated UiO-66 is notable for its highest ethanol yield. These differences are linked to the unique electronic structures and coordination environments of the metal particles, which influence the formation and stabilization of CO_2 reduction intermediates, thus affecting the selectivity and efficiency of the photoconver-

sion process [40]. The results underscore the importance of selecting appropriate metal decorations to optimize the photocatalytic reduction of CO_2 to liquid fuels.

^{1}H NMR analysis was conducted to quantify methanol and ethanol formation using the as-synthesized catalysts, and the corresponding NMR spectra are reported in Figure S4. Interestingly, the reaction catalyzed by the Pd@UiO-66 solution shows only one multiplet around 3.7 ppm, likely due to the decomposition of TEOA. In addition to the expected two peaks for TEOA, the NMR spectrum of the Au@UiO-66 reaction solution also shows an additional set of doublets of triplets at 3.93 ppm and 3.51 ppm, respectively, together with a doublet at 3.41 ppm and a small singlet at 9.52 ppm. This set of peaks is consistent with the degradation mechanism of TEOA reported by Li et al. [41], where TEOA in the presence of CO_2 can photochemically degrade to glycolaldehyde (a doublet and an aldehydic singlet) and diethanolamine (DEOA, the additional set of triplets).

Regarding the reaction products, all the NMR spectra are in agreement with their corresponding GC analysis. In this context, methanol was observed at 3.26 ppm (singlet), while ethanol was observed at 3.55 ppm (quartet) and 1.08 ppm (triplet). Additionally, all the reaction solutions presented traces of formate (singlet at 8.35 ppm), another typical reaction product of CO_2 reduction.

Based on the presented results and on similar systems reported in the literature, the following reaction mechanism is proposed here (Figure 8) [21,26,35]: in the photocatalytic CO_2 reduction to methanol (CH_3OH) and ethanol (C_2H_5OH) using Au@UiO-66, light absorption excites electrons in the UiO-66 framework, which are transferred to gold nanoparticles (Au NPs) on the surface. This transfer enhances electron mobility and facilitates CO_2 reduction. The photoexcited electrons reduce adsorbed CO_2 molecules to form reactive intermediates such as formate ($HCOO^-$) or acetate (CH_3COO^-), while the holes in UiO-66 oxidize water, producing protons (H^+) that participate in subsequent protonation steps.
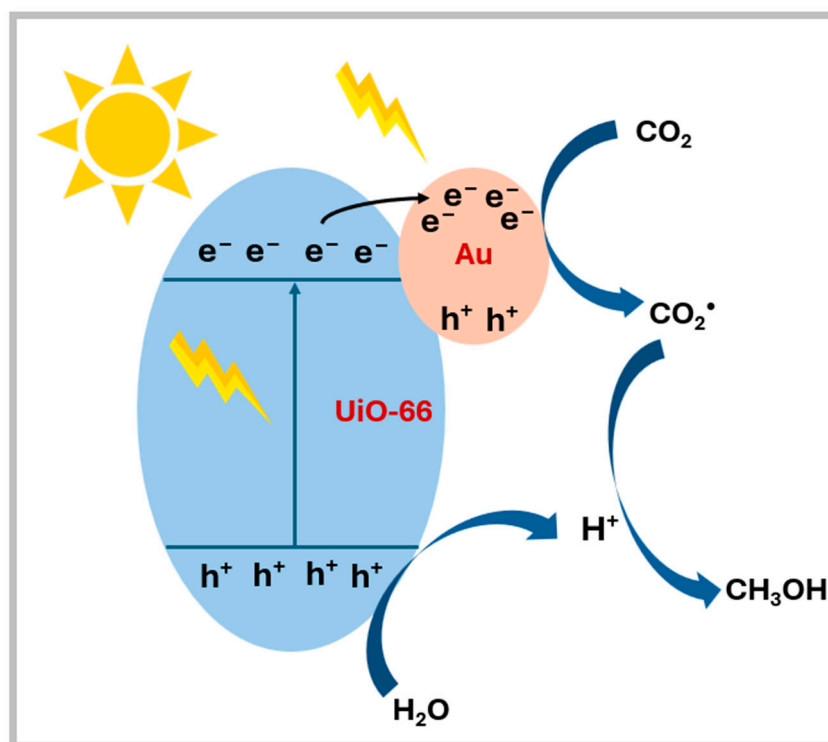
Figure 8. Proposed mechanism for CO_2 photocatalytic reduction over Au@UiO-66 catalyst.

The reaction mechanism begins with the formation of the CO_2 radical, represented by the reaction $CO_2 + e^- \rightarrow CO_2^{\cdot}$. This is followed by the formation of the formate

intermediate, where $CO_2^{\cdot}$ reacts with water and an electron to yield $HCOO^-$ and H_2. Concurrently, water oxidation occurs, producing H^+ and $OH^{\cdot}$ radicals. For methanol production, the formate intermediate undergoes further reduction and protonation, leading to methanol via the overall reaction $CO_2 + 6H^+ + 6e^- \rightarrow CH_3OH + H_2O$. For ethanol production, two CO_2 molecules couple via C–C bond formation. The resulting intermediate is protonated and reduced, yielding ethanol through the overall reaction $2CO_2 + 12H^+ + 12e^- \rightarrow C_2H_5OH + 3H_2O$.

Gold nanoparticles (Au NPs) play a pivotal role in the process. They act as electron sinks, stabilizing the transfer of photoexcited electrons from UiO-66. They also enhance light absorption through localized surface plasmon resonance (LSPR), which increases the efficiency of photocatalysis. Additionally, Au NPs facilitate the reduction and stabilization of reactive intermediates, ensuring the selective formation of liquid fuels. The UiO-66 framework complements this by providing a robust structure for CO_2 adsorption due to its high surface area and porosity. It also aids in the generation of protons via water oxidation, ensuring a continuous supply for the reduction process.

The overall photocatalytic process relies on the synergistic interaction of light, electrons, protons, and CO_2. The Au NPs significantly enhance electron transfer and light harvesting, while the UiO-66 framework supports CO_2 adsorption and proton generation. Together, these components enable the efficient conversion of CO_2 into valuable liquid fuels like methanol and ethanol through a well-orchestrated sequence of reactions. Further studies will dig deeper into the reaction mechanism by the adoption of electron paramagnetic resonance (EPR) spectroscopy and $^{13}CO_2$ gas as the reactant.

The results summarized in Table 3 underscore the versatility of photocatalysts for CO_2 reduction, with products ranging from methanol (CH_3OH) and ethanol (C_2H_5OH) to CO, CH_4, and formic acid (HCOOH). Traditional catalysts such as g-C_3N_4/ZnO and CeO_2/Bi_2MoO_6 demonstrate moderate activity, with methanol yields of 0.6 μmol g_{cat}^{-1} h^{-1} and 32.5 μmol g_{cat}^{-1} h^{-1}, respectively, under visible light. Meanwhile, heterojunction systems like Cu_2O/TiO_2 exhibit variable yields (12–70 μmol g_{cat}^{-1} h^{-1}), reflecting the challenge of optimizing catalyst design for consistent performance.

Metal–organic frameworks functionalized with active metals or complexes emerge as frontrunners in photocatalytic efficiency. For instance, Cu single atom/UiO-66-NH_2 achieved yields of 5.33 μmol g_{cat}^{-1} h^{-1} for methanol and 4.22 μmol g_{cat}^{-1} h^{-1} for ethanol, illustrating the potential of single-atom catalysts. Other MOF-based systems, such as (graphene nanoflakes/ZIF-67), delivered methanol and ethanol yields of 50.93 μmol g_{cat}^{-1} h^{-1} and 33.97 μmol g_{cat}^{-1} h^{-1}, respectively, showcasing the synergy between MOFs and graphitic components. Among the top performers, Au/ZIF-8 and Cu/ZIF-8 stand out, with extraordinary methanol yields of 2650 μmol g_{cat}^{-1} h^{-1} and 2240 μmol g_{cat}^{-1} h^{-1} under UV–visible light. When restricted to visible light, Au@UiO-66 in this study achieves a remarkable methanol yield of 656.54 μmol g_{cat}^{-1} h^{-1}, far surpassing comparable catalysts like Cu@UiO-66 (50.61 μmol g_{cat}^{-1} h^{-1}) and Ni@UiO-66 (43.48 μmol g_{cat}^{-1} h^{-1}). This highlights the significant role of gold nanoparticles in enhancing light absorption and catalytic efficiency within MOF matrices.

Other MOFs tailored for alternative products also demonstrate impressive selectivity and efficiency. For instance, Ag@MIL-101-Cr produced CO (808.2 μmol g_{cat}^{-1} h^{-1}) and CH_4 (427.5 μmol g_{cat}^{-1} h^{-1}), while LHP QDs@PCN-221(Fe) achieved a combined yield of 1559 μmol g_{cat}^{-1} h^{-1} for CO and CH_4. These results showcase the flexibility of MOFs in tailoring catalytic sites to target specific reaction pathways. Overall, the table highlights the outstanding potential of MOFs as photocatalysts, not only for their superior yields in methanol production but also for their versatility in enabling selective CO_2 reduction pathways.

Table 3. Examples of CO_2 reduction performance for traditional photocatalysts and MOFs.

Catalyst	Main Products	Main Products' Yield ($\mu mol\ g_{cat}^{-1}\ h^{-1}$)	Light Irradiation	Ref
g-C_3N_4/ZnO	CH_3OH	0.6	Visible	[42]
CeO_2/Bi_2MoO_6 (5C-BM)	CH_3OH	32.5	Visible	[43]
CeO_2	CH_3OH	5.1	Visible	[43]
Bi_2MoO_6	CH_3OH	17.6	Visible	[43]
Cu_2O/TiO_2	CH_3OH	12–70	Visible	[44]
Cu/Ti(H_2)	—	—	Visible	[45]
(g-CNQDs@MOF)	—	386	Visible	[46]
Cu SAs/UiO-66-NH2	CH_3OH and C_2H_5OH	5.33; 4.22	Visible	[35]
Ag@Co-MOF-74	CO and H_2	CO ≈ 4.2 μmol H_2 ≈ 7.5 μmol	Visible	[47]
Ag@MIL-101-Cr	CO and CH_4	CO = 808.2 CH_4 = 427.5	Visible	[48]
Pt@MIL-125(Ti)	$HCOO^-$ and H_2	H_2 = 235 μmol $HCOO^-$ = 13 μmol	Visible	[49]
Pt@NH_2-UiO-68	CO	400	Visible	[50]
Ag⊂Re3-MOF	CO	0.093	Visible	[31]
Cp*Rh@UiO-67	H_2 and $HCOO^-$	$HCOO^-$ = 0.9 μmol h^{-1} H_2 = 1.2 μmol h^{-1}	Visible	[51]
LHP QDs@PCN-221(Fe)	CO and CH_4	1559 CO (34%)/CH_4 (66%)	Visible	[52]
(GNF(X)/ZIF-67)	CH_3OH and C_2H_5OH	CH_3OH = 50.93 C_2H_5OH = 33.97	Visible	[53]
Au/PPF-3	HCOOH	42.7	Visible	[54]
Au/ZIF-8	CH_3OH	2650	UV/Visible	[55]
Cu/ZIF-8	CH_3OH	2240	UV/Visible	[55]
Au@ZIF-67	CO	0.04	Visible	[56]
Au@UiO-66	CH_3OH	656.54	Visible	This work
Cu@UiO-66	CH_3OH	50.61	Visible	This work
Ni@UiO-66	CH_3OH	43.48	Visible	This work

3. Materials and Methods

3.1. Materials

All chemicals were purchased from commercial suppliers and used without further purification as follows: zirconium (IV) chloride ($ZrCl_4$, Alfa Aesar, Ward Hill, MA, USA, 99.5+%), benzene-1,4-dicarboxylic acid (BDC, $C_8H_6O_4$, Sigma Aldrich, Louis, MO, USA, 98%), N,N-Dimethyl formamide (DMF, C_3H_7NO, Honeywell, Muskegon, MI, USA, ≥99.9%), methanol (CH_3OH, Fisher Scientific, Loughborough, UK, ≥99.5%), hydrogen tetrachloroaurate-(III) hydrate ($HAuCl_4 \cdot H_2O$, Alfa Aesar, Ward Hill, MA, USA, 99.9%), silver nitrate ($AgNO_3$, Sigma Aldrich, Louis, MO, USA, 99.9999%), palladium (II) acetate ($[Pd(OAc)_2]_3$, Sigma Aldrich, Louis, MO, USA, ≥99.9%), copper (II) chloride dihydrate ($CuCl_2 \cdot 2H_2O$, Sigma Aldrich, Louis, MO, USA, 99+%), chloroplatinic acid hydrate ($H_2PtCl_6 \cdot H_2O$, Sigma Aldrich, Louis, MO, USA, 38%), nickel (II) chloride hexahydrate

($NiCl_2 \cdot 6H_2O$, Alfa Aesar, Ward Hill, MA, USA, 98%), and sodium borohydride ($NaBH_4$, Sigma Aldrich, Louis, MO, USA, $\geq$98.0%).

3.2. Material Synthesis

3.2.1. UiO-66 Synthesis

A quantity of 1.16 g of $ZrCl_4$ was mixed with 0.83 g of BDC in 30 mL of DMF. The mixture was stirred for 30 min, then transferred into a 100 mL Teflon autoclave and heated at 140 °C in an oven for 24 h.

3.2.2. NPs@UiO-66 Synthesis

Targeting a 1% loading of metal on the UiO-66 support, 30 mg of $HAuCl_4 \cdot H_2O$, $AgNO_3$, $[Pd(OAc)_2]_3$, $CuCl_2 \cdot 2H_2O$, $H_2PtCl_6 \cdot H_2O$, or $NiCl_2 \cdot 6H_2O$ in 15 mL of methanol were added, respectively, to 300 mg of UiO-66 in 40 mL of methanol dropwise while stirring at room temperature overnight under a nitrogen atmosphere. After that, 100 mg of $NaBH_4$ in 10 mL of methanol was added dropwise while stirring for 2 h at room temperature. Next, the mixture was filtered, washed with methanol, and dried under air for 1 h.

3.3. Photocatalytic CO_2 Reduction Setup and Performance

A continuous-flow system (0.1 L m^{-1}) was used to evaluate the performance of the photocatalytic CO_2 reduction reaction. A 300 W Xe lamp (ASAHI SPECTRA, Torrance, CA, USA) was used as the visible light source at 385–740 nm with an intensity of 420 W/m^2. Following a typical procedure, 0.1 g of photocatalyst was dispersed in 50 mL of deionized water, along with 100 μL of triethanolamine (TEOA), and it was mixed using magnetic stirring. Prior to irradiation, CO_2 gas with a purity of 99.999% was bubbled through the suspension for 30 min. The reaction temperature was maintained at approximately 10 °C using an ice bath. The liquid products were analyzed for the quantification of ethanol and methanol by an Agilent 7890B GC system equipped with a flame ionization detector (FID) and headspace sampling system (Agilent Technologies, Santa Clara, CA, USA). The chromatographic separation was performed on a CP Wax 57 CB column of 50 m length, 0.25 mm i.d., and 0.25 μm film thickness. The sample (6 mL) was added into 20 mL of headspace vial, which was immediately sealed with an aluminum cap lined with PTFE/silicone septum. The conditions for headspace were as follows: sample equilibration for 20 min at 60 °C without shaking, vial pressurization time of 0.15 min, sample loop fill time of 0.15 min, with loop and transfer line temperature at 90 °C. All the injections were made in the split mode (10:1). The oven temperature was 40 °C (held for 4 min), increased by 10 °C/min to 90 °C, followed by 15 °C/min ramping to reach 135 °C (held for 2 min). The inlet and detector temperatures were 250 °C and 300 °C, respectively. Helium (99.9999%) was used as the carrier gas, with a constant flow of 2 mL/min. The air and hydrogen flow rates were 400 and 40 mL/min, respectively. The GC data were analyzed using OpenLab CDS ChemStation software (Agilent Technologies, version A.02.05.021). Each sample was analyzed in duplicate.

The quantification of ethanol and methanol in the liquid products was also carried out using ^{1}H NMR spectroscopy. All NMR measurements were performed at 298 K on a standard bore 800 MHz (18.8 T) Bruker AVANCE III HD spectrometer running TopSpin 3.6 and equipped with a Z-gradient 5 mm BBO H&F Bruker cryoprobe (Bruker, Ettlingen, Germany). The ^{1}H NMR spectra were collected at a ^{1}H Larmor frequency of 800.13 MHz using the water suppression one-dimensional pulse sequence of excitation sculpting with gradients using a perfect echo [57,58]. As in a typical procedure, 540 μL of sample aliquots were mixed with 60 μL of D_2O solution containing 2.0 mM of sodium acetate as an internal standard. The transmitter offset was set at the water signal (~4.7 ppm), and 256 transients were typically collected with an optimized relaxation delay of 10s and an acquisition time of

3 s. The acquired data were processed with first-order zero filling and a 0.2 Hz exponential line broadening function.

3.4. Characterization

X-ray powder diffraction (XRD) was conducted to examine the crystal structure of the as-prepared catalyst by an X-ray diffractor (XRD-6100x, Shimadzu, Kyoto, Japan) using Cu-Kα (λ = 1.5406 Å) radiation at 40 kV and 30 mA and a scanning speed of 7°/min, ranging from 10° to 70°. Field emission scanning electron microscopy (FESEM) and energy dispersive X-ray spectroscopy (EDS) were performed by (FEI Quanta650FEG SEM) for imaging and (Quantax400 EDS, Bruker) for microanalysis to investigate the surface morphology and elemental composition. The morphology was further investigated by transmission electron microscopy (TEM) using a transmission electron microscope (JEOL 2010, JEOL, Tokyo, Japan) operated at 200 kV. The samples were prepared by dispersing them in ethanol, and droplets of the resulting suspension were placed onto a thin copper grid. Following the vaporization of ethanol, the thin copper grid was introduced into the sample chamber of the transmission electron microscope. Furthermore, specific BET surface areas of the as-prepared catalysts were measured by a surface area analyzer (ASAP 2420, Micromeritics, Norcross, GA, USA) at 77 K. Before measurements, samples were dried at 90 °C for 30 min followed by degassing at 150 °C for 6 h under vacuum to remove CO_2, water, and any other impurities. The specific surface area was calculated by the BET equation and BJH desorption for pore size analysis. To determine the binding energies and chemical states of the grown structures, X-ray photoelectron spectroscopy (XPS) was performed on the standard Thermal-fisher ESCALAB 250XI-type XPS platform (Thermo Fisher Scientific, Waltham, MA, USA). A monochromatic Ag Kα anode X-ray beam was used with a beam energy of 1486.6 eV and an energy resolution better than 100 meV. The XPS spectra are acquired with a 180° hemispherical electron energy analyzer with a normal emission angle and a beam incident angle of 45° to the surface normal. High-resolution core level spectra are taken with a pass energy of 20 eV and a step size of 0.02 eV. Sample spectra were also collected after an etching process by an Ar$^+$ beam under an ion energy of 4000 kV and a raster size of 1.5 mm.

4. Conclusions

Understanding the chemistry and physics of the photoconversion of CO_2 is a complex matter that requires a deep analysis of all the morphological as well as electronic aspects of the catalysts. Indeed, the results reported in this work stem from a synergistic effect of combining UiO-66 and metal/plasmonic NPs, which enhances the overall photocatalytic performance. The high surface area and large porosity of UiO-66 provide an ideal environment for the dispersion of metal NPs, facilitating better interaction between light, the photocatalyst, and CO_2 molecules. The active sites or active species for photocatalytic CO_2 reduction on the metal–UiO-66 MOF include the metal nanoparticles and the unsaturated metal sites within the UiO-66 framework. The metal NPs serve as catalytic centers for electron transfer, stabilizing intermediates such as $CO_2^{\cdot}$ and promoting selective product formation. Additionally, the UiO-66 framework provides Lewis acidic zirconium nodes that enhance CO_2 adsorption and activation, facilitating the formation of reactive intermediates like COOH* and CHO*, which are essential for the formation of methanol and ethanol.

The integration of plasmonic metal nanoparticles (NPs) such as Au and Cu into the UiO-66 framework has significantly enhanced the photocatalytic reduction of CO_2 to methanol and ethanol. The improved performance can be attributed to several key mechanisms, each playing a critical role in the observed catalytic activity. The incorporation of plasmonic NPs introduces localized surface plasmon resonance effects, contributing to

higher light absorption and effective charge carrier dynamics. These fields can increase the generation of electron–hole pairs and improve the efficiency of charge separation. Furthermore, the presence of metal NPs facilitates the separation of photogenerated electron–hole pairs, reducing the recombination rate. This efficient charge separation is crucial for enhancing the photocatalytic activity. Then, the electrons can be transferred to the CO_2 molecules adsorbed on the MOF surface, thus promoting the reduction reactions. Future work should focus on a deeper understanding of the reaction mechanism for Au@UiO-66 by combining advanced spectroscopical characterization, as well as exploring the effect of metal loading on the photocatalytic performance.

Supplementary Materials: The following supporting information can be downloaded at: https://www.mdpi.com/article/10.3390/catal15010070/s1. Figure S1: SEM Images of Metal-Functionalized UiO-66 Samples: (a) Au@UiO-66, (b) Cu@UiO-66, (c) Ag@UiO-66, (d) Pd@UiO-66, (e) Pt@UiO-66, and (f) Ni@UiO-66. Figure S2: EDS Chemical Spectra of Metal-Functionalized UiO-66: (a) Au@UiO-66, (b) Cu@UiO-66, (c) Ag@UiO-66, (d) Pd@UiO-66, (e) Pt@UiO-66, and (f) Ni@UiO-66. Figure S3. Tauc Plots of Investigated Metal-Organic Framework (MOF) Samples for Band Gap Analysis. Figure S4: ^{1}H NMR Spectra of Reaction Solutions Catalyzed by: (a) UiO-66, (b) Au@UiO-66, (c) Cu@UiO-66, (d) Ag@UiO-66, (e) Pd@UiO-66, (f) Pt@UiO-66, and (g) Ni@UiO-66.

Author Contributions: Conceptualization, A.S. and B.A.; methodology, A.A. (Ahmed Abotaleb), M.A., K.M. and A.S.; validation, A.S. and B.A.; formal analysis, A.A. (Ahmed Abotaleb), M.A. and K.M.; investigation, A.E., Z.T., A.A.-Y. and A.A. (Alaa Alkhateeb); writing—original draft preparation, A.E., Z.T., A.S., K.M., B.A., A.A. (Ahmed Abotaleb) and M.A.; supervision, A.S.; funding acquisition, B.A. All authors have read and agreed to the published version of the manuscript.

Conflicts of Interest: The authors declare no conflicts of interest.

References

1. Karimi, M.; Mehrabadi, Z.; Farsadrooh, M.; Bafkary, R.; Derikvandi, H.; Hayati, P.; Mohammadi, K. Metal–organic framework. *Interface Sci. Technol.* **2021**, *33*, 279–387.
2. Safaei, M.; Foroughi, M.M.; Ebrahimpoor, N.; Jahani, S.; Omidi, A.; Khatami, M. A review on metal-organic frameworks: Synthesis and applications. *TrAC Trends Anal. Chem.* **2019**, *118*, 401–425. [CrossRef]
3. Yusuf, V.F.; Malek, N.I.; Kailasa, S.K. Review on Metal-Organic Framework Classification, Synthetic Approaches, and Influencing Factors: Applications in Energy, Drug Delivery, and Wastewater Treatment. *ACS Omega* **2022**, *7*, 44507–44531. [CrossRef]
4. Zhou, H.C.; Long, J.R.; Yaghi, O.M. Introduction to metal-organic frameworks. *Chem. Rev.* **2012**, *112*, 673–674. [CrossRef]
5. Dutta, A.; Pan, Y.; Liu, J.Q.; Kumar, A. Multicomponent isoreticular metal-organic frameworks: Principles, current status and challenges. *Coord. Chem. Rev.* **2021**, *445*, 214074. [CrossRef]
6. Sakamaki, Y.; Tsuji, M.; Heidrick, Z.; Watson, O.; Durchman, J.; Salmon, C.; Burgin, S.R.; Hassan Beyzavi, M. Preparation and Applications of Metal–Organic Frameworks (MOFs): A Laboratory Activity and Demonstration for High School and/or Undergraduate Students. *J. Chem. Educ.* **2020**, *97*, 1109. [CrossRef]
7. Bindra, A.K.; Wang, D.; Zhao, Y. Metal–Organic Frameworks Meet Polymers: From Synthesis Strategies to Healthcare Applications. *Adv. Mater.* **2023**, *35*, 2300700. [CrossRef]
8. Raptopoulou, C.P. Metal-Organic Frameworks: Synthetic Methods and Potential Applications. *Materials* **2021**, *14*, 310. [CrossRef]

9.   Scott Meek, B.T.; Greathouse, J.A.; Allendorf, M.D.; Meek, S.T.; Allendorf, M.D.; Greathouse, J.A. Metal-Organic Frameworks: A Rapidly Growing Class of Versatile Nanoporous Materials. *Adv. Mater.* **2011**, *23*, 249–267. [CrossRef]

10. Kumar, S.; Vijayan, S.; Goyal, K.; Kathuria, M.; Gulati, S. Functionalization Strategies of Metal–Organic Frameworks (MOFs): Diverse Ways to Versatile MOFs. In *Metal-Organic Frameworks (MOFs) as Catalysts*; Springer: Singapore, 2022; pp. 99–123.

11. Wang, H.; Li, J.; Zhang, Z. Metal-organic frameworks embedded with nanoparticles for CO_2 capture and conversion. In *Nanomaterials for Carbon Dioxide Capture and Conversion Technologies*; Elsevier: Amsterdam, The Netherlands, 2022; pp. 261–275.

12. Khan, M.; Akmal, Z.; Tayyab, M.; Mansoor, S.; Zeb, A.; Ye, Z.; Zhang, J.; Wu, S.; Wang, L. MOFs materials as photocatalysts for CO_2 reduction: Progress, challenges and perspectives. *Carbon Capture Sci. Technol.* **2024**, *11*, 100191. [CrossRef]

13. Liu, Y.; Guo, H.; Sun, Z.; Li, T.; Qian, J.; Wang, L.; Zhang, J.; Zhang, Z. Recent advances in amino-functionalized metal–organic frameworks for sustainable photocatalytic carbon dioxide reduction. *Sep. Purif. Technol.* **2025**, *360*, 131023. [CrossRef]

14. Khan, M.M.; Rahman, A.; Matussin, S.N. Recent Progress of Metal-Organic Frameworks and Metal-Organic Frameworks-Based Heterostructures as Photocatalysts. *Nanomaterials* **2022**, *12*, 2820. [CrossRef]

15. Mukherjee, D.; Van der Bruggen, B.; Mandal, B. Advancements in visible light responsive MOF composites for photocatalytic decontamination of textile wastewater: A review. *Chemosphere* **2022**, *295*, 133835. [CrossRef]

16. Wang, L.; Hasanzadeh Kafshgari, M.; Meunier, M.; Wang, L.; Hasanzadeh Kafshgari, M.; Meunier, M. Optical Properties and Applications of Plasmonic-Metal Nanoparticles. *Adv. Funct. Mater.* **2020**, *30*, 2005400. [CrossRef]

17. Chang, H.; Rho, W.Y.; Son, B.S.; Kim, J.; Lee, S.H.; Jeong, D.H.; Jun, B.H. Plasmonic Nanoparticles: Basics to Applications (I). *Adv. Exp. Med. Biol.* **2021**, *1309*, 133–159.

18. Tudor, M.; Borlan, R.; Maniu, D.; Astilean, S.; de la Chapelle, M.L.; Focsan, M. Plasmon-enhanced photocatalysis: New horizons in carbon dioxide reduction technologies. *Sci. Total Environ.* **2024**, *932*, 172792. [CrossRef]

19. Harris, N.; Blaber, M.G.; Schatz, G.C. Optical Properties of Metal Nanoparticles. In *Encyclopedia of Nanotechnology*; Bhushan, B., Ed.; Springer: Dordrecht, The Netherlands, 2016; pp. 3027–3048.

20. Koh, C.S.L.; Sim, H.Y.F.; Leong, S.X.; Boong, S.K.; Chong, C.; Ling, X.Y. Plasmonic Nanoparticle-Metal-Organic Framework (NP-MOF) Nanohybrid Platforms for Emerging Plasmonic Applications. *ACS Mater. Lett.* **2021**, *3*, 557–573. [CrossRef]

21. Zhao, Z.; Ren, G.; Meng, X.; Li, Z. Au Nanoparticle-Loaded UiO-66 Metal–Organic Framework for Efficient Photocatalytic N2 Fixation. *Processes* **2024**, *12*, 64. [CrossRef]

22. Ameta, R.; Panchal, S.; Ameta, N.; Ameta, S.C. Photocatalytic reduction of carbon dioxide. *Mater. Sci. Forum* **2013**, *764*, 83–96. [CrossRef]

23. Derichter, R.K.; Ming, T.; Caillol, S. Fighting global warming by photocatalytic reduction of CO_2 using giant photocatalytic reactors. *Renew. Sustain. Energy Rev.* **2013**, *19*, 82–106. [CrossRef]

24. Akhter, P.; Farkhondehfal, M.A.; Hernández, S.; Hussain, M.; Fina, A.; Saracco, G.; Khan, A.U.; Russo, N. Environmental issues regarding CO_2 and recent strategies for alternative fuels through photocatalytic reduction with titania-based materials. *J. Environ. Chem. Eng.* **2016**, *4*, 3934–3953. [CrossRef]

25. Olivo, A.; Signoretto, M.; Ghedini, E. CO_2 photoreduction to solar fuels: Basis effect on TiO_2 photocataiysts. *DGMK Tagungsbericht* **2017**, *2017*, 137–143.

26. Li, L.; Jung, H.S.; Lee, J.W.; Kang, Y.T. Review on applications of metal–organic frameworks for CO_2 capture and the performance enhancement mechanisms. *Renew. Sustain. Energy Rev.* **2022**, *162*, 112441. [CrossRef]

27. Chebbi, A.; Sinopoli, A.; Abotaleb, A.; Bicer, Y. Photocatalytic conversion of carbon dioxide, methane, and air for green fuels synthesis. *Catal. Sci. Technol.* **2023**, *13*, 4895–4918. [CrossRef]

28. Li, X.; Wang, L.; Xing, Y.; Su, W. Research progress in photo/electrocatalytic reduction of CO_2 by functionalized metal-organic frameworks. *Sustain. Energy Fuels* **2022**, *6*, 3516–3526. [CrossRef]

29. Chang, X.L.; Yan, T.; Pan, W.G. Toward Tailoring Metal-Organic Frameworks for Photocatalytic Reduction of CO_2 to Fuels. *Cryst. Growth Des.* **2024**, *24*, 2619–2644. [CrossRef]

30. Dao, X.Y.; Sun, W.Y. Single- and mixed-metal–organic framework photocatalysts for carbon dioxide reduction. *Inorg. Chem. Front.* **2021**, *8*, 3178–3204. [CrossRef]

31. Choi, K.M.; Kim, D.; Rungtaweevoranit, B.; Trickett, C.A.; Barmanbek, J.T.D.; Alshammari, A.S.; Yang, P.; Yaghi, O.M. Plasmon-enhanced photocatalytic CO_2 conversion within metal-organic frameworks under visible light. *J. Am. Chem. Soc.* **2017**, *139*, 356–362. [CrossRef]

32. Robatjazi, H.; Weinberg, D.; Swearer, D.F.; Jacobson, C.; Zhang, M.; Tian, S.; Zhou, L.; Nordlander, P.; Halas, N.J. Metal-organic frameworks tailor the properties of aluminum nanocrystals. *Sci. Adv.* **2019**, *5*. [CrossRef]

33. Winarta, J.; Shan, B.; McIntyre, S.M.; Ye, L.; Wang, C.; Liu, J.; Mu, B. A Decade of UiO-66 Research: A Historic Review of Dynamic Structure, Synthesis Mechanisms, and Characterization Techniques of an Archetypal Metal–Organic Framework. *Cryst. Growth Des.* **2020**, *20*, 1347–1362.

34. Liu, H.; Cheng, M.; Liu, Y.; Zhang, G.; Li, L.; Du, L.; Li, B.; Xiao, S.; Wang, G.; Yang, X. Modified UiO-66 as photocatalysts for boosting the carbon-neutral energy cycle and solving environmental remediation issues. *Coord. Chem. Rev.* **2022**, *458*, 214428. [CrossRef]

35. Wang, G.; He, C.T.; Huang, R.; Mao, J.; Wang, D.; Li, Y. Photoinduction of Cu Single Atoms Decorated on UiO-66-NH2 for Enhanced Photocatalytic Reduction of CO_2 to Liquid Fuels. *J. Am. Chem. Soc.* **2020**, *142*, 19339–19345. [CrossRef]

36. Ganesh, I. Conversion of carbon dioxide into methanol—A potential liquid fuel: Fundamental challenges and opportunities (a review). *Renew. Sustain. Energy Rev.* **2014**, *31*, 221–257. [CrossRef]

37. Zheng, G.; Pastoriza-Santos, I.; Pérez-Juste, J.; Liz-Marzán, L.M. Plasmonic metal-organic frameworks. *SmartMat* **2021**, *2*, 446–465. [CrossRef]

38. Wang, F.-F.; Liang, F.; Zhang, Y.; Chen, X.; Chen, D.-L.; Zhu, W. Stabilities and Electronic Structures of Transition Metal (Cu, Ag, Au, Ni, Pd, Pt) Cluster-Confined UiO-66. *J. Phys. Chem. C* **2020**, *124*, 28123–28131. [CrossRef]

39. Andrade, P.H.M.; Volkringer, C.; Loiseau, T.; Tejeda, A.; Hureau, M.; Moissette, A. Band gap analysis in MOF materials: Distinguishing direct and indirect transitions using UV–vis spectroscopy. *Appl. Mater. Today* **2024**, *37*, 102094. [CrossRef]

40. Li, D.; Hao, C.; Liu, H.; Zhang, R.; Li, Y.; Guo, J.; Vilancuo, C.C.; Guo, J. Photocatalytic CO_2 Conversion to Ethanol: A Concise Review. *Catalysts* **2022**, *12*, 1549. [CrossRef]

41. Li, Z.; Yang, C.; Su, Y.; Cheng, Y.; Cui, Y.; Liu, S.; Fang, Y. Photochemical reduction of CO_2 into CO coupling with triethanolamine decomposition. *RSC Adv.* **2023**, *13*, 31616–31621. [CrossRef]

42. Yu, W.; Xu, D.; Peng, T. Enhanced photocatalytic activity of g-C3N4 for selective CO_2 reduction to CH_3OH via facile coupling of ZnO: A direct Z-scheme mechanism. *J. Mater. Chem. A* **2015**, *3*, 19936–19947. [CrossRef]

43. Dai, W.; Hu, X.; Wang, T.; Xiong, W.; Luo, X.; Zou, J. Hierarchical CeO_2/Bi_2MoO_6 heterostructured nanocomposites for photoreduction of CO_2 into hydrocarbons under visible light irradiation. *Appl. Surf. Sci.* **2018**, *434*, 481–491. [CrossRef]

44. Cheng, S.-P.; Wei, L.-W.; Wang, H.-P. Photocatalytic Reduction of CO_2 to Methanol by Cu_2O/TiO_2 Heterojunctions. *Sustainability* **2022**, *14*, 374. [CrossRef]

45. Xi, H.; Xu, Y.; Zou, W.; Ji, J.; Cai, Y.; Wan, H.; Dong, L. Enhanced methanol selectivity of $CuxO/TiO_2$ photocatalytic CO_2 reduction: Synergistic mechanism of surface hydroxyl and low-valence copper species. *J. CO2 Util.* **2022**, *55*, 101825. [CrossRef]

46. Sonowal, K.; Nandal, N.; Basyach, P.; Kalita, L.; Jain, S.L.; Saikia, L. Photocatalytic reduction of CO_2 to methanol using Zr(IV)-based MOF composite with g-C3N4 quantum dots under visible light irradiation. *J. CO2 Util.* **2022**, *57*, 101905. [CrossRef]

47. Deng, X.; Yang, L.; Huang, H.; Yang, Y.; Feng, S.; Zeng, M.; Li, Q.; Xu, D. Shape-Defined Hollow Structural Co-MOF-74 and Metal Nanoparticles@Co-MOF-74 Composite through a Transformation Strategy for Enhanced Photocatalysis Performance. *Small* **2019**, *15*, 1902287. [CrossRef]

48. Guo, F.; Yang, S.; Liu, Y.; Wang, P.; Huang, J.; Sun, W.-Y. Size Engineering of Metal–Organic Framework MIL-101(Cr)–Ag Hybrids for Photocatalytic CO_2 Reduction. *ACS Catal.* **2019**, *9*, 8464–8470. [CrossRef]

49. Sun, D.; Liu, W.; Fu, Y.; Fang, Z.; Sun, F.; Fu, X.; Zhang, Y.; Li, Z. Noble metals can have different effects on photocatalysis over metal-organic frameworks (MOFs): A case study on M/NH_2-MIL-125(Ti) (M=Pt and Au). *Chem. (Weinh. Der Bergstr. Ger.)* **2014**, *20*, 4780–4788. [CrossRef]

50. Guo, F.; Wei, Y.-P.; Wang, S.-Q.; Zhang, X.-Y.; Wang, F.-M.; Sun, W.-Y. Pt nanoparticles embedded in flowerlike NH2-UiO-68 for enhanced photocatalytic carbon dioxide reduction. *J. Mater. Chem. A* **2019**, *7*, 26490–26495. [CrossRef]

51. Chambers, M.B.; Wang, X.; Elgrishi, N.; Hendon, C.H.; Walsh, A.; Bonnefoy, J.; Canivet, J.; Quadrelli, E.A.; Farrusseng, D.; Mellot-Draznieks, C.; et al. Photocatalytic Carbon Dioxide Reduction with Rhodium-based Catalysts in Solution and Heterogenized within Metal–Organic Frameworks. *ChemSusChem* **2015**, *8*, 603–608. [CrossRef]

52. Wu, L.-Y.; Mu, Y.-F.; Guo, X.-X.; Zhang, W.; Zhang, Z.-M.; Zhang, M.; Lu, T.-B. Encapsulating Perovskite Quantum Dots in Iron-Based Metal–Organic Frameworks (MOFs) for Efficient Photocatalytic CO_2 Reduction. *Angew. Chem. Int. Ed.* **2019**, *58*, 9491–9495. [CrossRef]

53. Manna, R.; Bhattacharya, G.; Raj, S.; Samanta, A.N. Boosting photocatalytic CO_2 reduction efficiency by graphene nanoflakes (GNF) decorated ZIF-67 under visible light irradiation. *J. Environ. Chem. Eng.* **2024**, *12*, 111722. [CrossRef]

54. Chen, L.; Wang, Y.; Yu, F.; Shen, X.; Duan, C. A simple strategy for engineering heterostructures of Au nanoparticle-loaded metal–organic framework nanosheets to achieve plasmon-enhanced photocatalytic CO_2 conversion under visible light. *J. Mater. Chem. A* **2019**, *7*, 11355–11361. [CrossRef]

55. Izadpanah Ostad, M.; Niknam Shahrak, M.; Galli, F. The effect of different reaction media on photocatalytic activity of Au- and Cu-decorated zeolitic imidazolate Framework-8 toward CO_2 photoreduction to methanol. *J. Solid State Chem.* **2022**, *315*, 123514. [CrossRef]

56. Tian, T.; Xu, J.; Abdolazizi, A.; Ji, C.; Hou, J.; Riley, D.J.; Yan, C.; Ryan, M.P.; Xie, F.; Petit, C. A monolithic gold nanoparticle@metal-organic framework composite as CO_2 photoreduction catalyst. *Mater. Today Nano* **2023**, *21*, 100293. [CrossRef]

57.   Adams, R.W.; Holroyd, C.M.; Aguilar, J.A.; Nilsson, M.; Morris, G.A. "Perfecting" WATERGATE: Clean proton NMR spectra from aqueous solution. *Chem. Commun.* **2012**, *49*, 358–360. [CrossRef] [PubMed]

58.   Hwang, T.L.; Shaka, A.J. Water Suppression That Works. Excitation Sculpting Using Arbitrary Wave-Forms and Pulsed-Field Gradients. *J. Magn. Reson. Ser. A* **1995**, *112*, 275–279. [CrossRef]